Development of an automated non-axisymmetric endwall contour design system for the rotor of a 1-stage research turbine – part 1: System design

3 authors, including:

Jonathan Bergh
University of Cape Town
8 PUBLICATIONS **5** CITATIONS

Gc Snedden
Council for Scientific and Industrial Research, South Africa
40 PUBLICATIONS **92** CITATIONS

Some of the authors of this publication are also working on these related projects:

Master's Thesis View project

Investigation into the effect of build direction on fatigue and fracture properties of SLM nickel-based super alloy used for the manufacture of high speed gas turbine blades View project

Development of an automated non-axisymmetric endwall contour design system for the rotor of a 1-stage research turbine - Part 1 System Design

Jonathan Bergh[1], Glen Snedden[2] and Daya Reddy[1]

Abstract

Secondary flows are a well-known source of loss in turbomachinery flows, contributing up to 30% of the total aerodynamic blade row loss. With the increase in pressure on aero-engine manufacturers to produce lighter, more powerful and increasingly more efficient engines, the mitigation of the losses associated with secondary flow has become significantly more important than in the past. This is because the production of secondary flow is closely related to the amount of loading and hence work output of a blade row, which then allows part counts and overall engine weight to be reduced. Similarly, higher efficiency engines demand larger engine pressure ratios which in turn lead to reduced blade passage heights in which secondary flows then dominate. This article discusses the design and application of an automated turbine *non-axisymmetric endwall contour* optimization procedure for the rotor of a low speed, 1-stage research turbine, which was used as part of a research program to determine the most effective objective functions for reducing turbine secondary flows. In order to produce as effective as possible designs, the optimization procedure was coupled to a CFD routine with as high a degree of fidelity as possible and an efficient global optimization scheme based on the so-called *EGO* algorithm. In order to compliment the requirements of the *EGO* approach, as well as offset some of the computational requirements of the CFD, the DACE metamodel was used as an underlying surrogate model.

Keywords

kriging, DACE, EGO, turbine optimization, non-axisymmetric endwalls

Introduction

Secondary flows occur where ever a fluid of non-uniform vorticity is turned. In gas turbines, this occurs when the inlet boundary layer of the working fluid passes through the curved passages of the compressor and turbine blade rows where, because of the relative velocity difference between the flow at the pressure and suction sides of adjacent blades, the inlet vorticity vector (Ω_1) is reorientated to include a component in the streamwise direction (Ω_{s2}) at the blade row exit (Fig. 1).

More physically, secondary flows can be understood to originate as a result of the pressure gradients which form within the blade rows of a turbine (or compressor) due to the reaction forces set up by the blades to turn the flow. These pressure gradients, which then are subsequently imposed on the low momentum fluid of the endwall boundary layer, cause this low momentum fluid to be forced across the blade passages in the direction of the adjacent blades where they are then seen to impinge upon the suction surface of the adjacent blade. Upon doing this, this fluid is then seen to separate from the endwall and travel up the blade suction surface, which then results (as a consequence of mass conservation), in a return flow further away from the endwall, giving rise to a streamwise vortex which is then convected downstream of the blade row. An overall view of the secondary flow structures is shown in Fig. 2.

Because of the well defined relationship between flow turning and the cross passage pressure gradients, there is
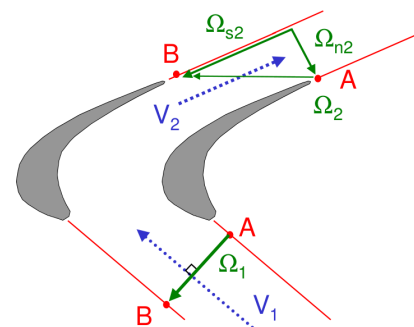
Figure 1. Generation of streamwise vorticity (Ω_{s2}) due to the turning of the inlet vorticity vector (Ω_1) (Reproduced from Ingram[1])

therefore a natural link between the degree of aerodynamic loading of a blade row and the magnitude of the secondary flow it generates. Trends in turbomachinery design towards reducing engine weight (and therefore part counts), while at the same time requiring maintained or even greater power outputs, have resulted in modern day engines with fewer
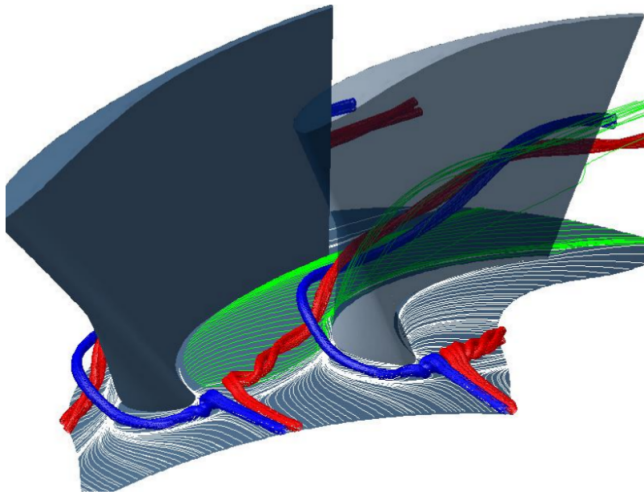
[1]CERECAM, University of Cape Town, South Africa
[2]Aeronautical Systems, CSIR, South Africa

Corresponding author:
Jonathan Bergh, CERECAM, University of Cape Town, Cape Town, South Africa
Email: jonathan.bergh@uct.ac.za

Figure 2. The principal components of turbine secondary flow (Reproduced from Snedden[2])

blades and higher individual blade loadings and therefore increase flow turning in individual blade rows. Combined with an increased pressure on engine manufacturers to produce more efficient and environmentally friendly engines (and therefore more efficiency), these trends have resulted in a situation where the mitigation of *endwall* or *secondary loss* associated with the secondary flows, is considerably more important than was previously the case.

Non-axisymmetric endwall contouring

Non-axisymmetric endwall contouring is a well-known but somewhat controversial technique which was developed originally for the reduction of the losses associated with turbine disc leakage flows[3] by reducing the pressure variations at the exit of each blade row, although following the discovery of reductions in the secondary flow during that investigation, it has been developed almost exclusively as a method for the mitigation of secondary loss (see[4–8]).

In essence, non-axisymmetric endwall contouring works by allowing the shape of the endwalls of the turbine hub or shroud to depart from that of a cylinder, and instead, take on non-axisymmetric or three-dimensional curvature. As a result of this and therefore the curvature of the streamlines in the vicinity of the contoured endwalls, non-axisymmetric endwalls can be used to manipulate the local endwall pressure field and consequently reduce the static pressure gradients which were described above as being the principal driving force of the secondary flows.

Prediction of secondary loss and loss 'proxies'

Many authors have described the inability of existing computational fluid dynamics (CFD) codes to predict the secondary loss (i.e. the losses associated with the secondary flows) with sufficient accuracy for it to be used *directly* in the design of non-axisymmetric endwall contours[4,6]. As a result of this, the use of so-called *proxies* for the secondary loss have become commonplace in non-axisymmetric endwall design and optimization routines, although a few authors[9,10] have claimed successful use of the coefficient of total pressure loss within the literature. As a result, to date there exists a wide variety of measures which have been

developed for identification and minimization of secondary flows in non-axisymmetric endwall contours. Further, the independent nature of many of the efforts related to endwall design research, has resulted in considerable debate relating to the efficacy of many of these quantities.

Table 1 gives an indication of the variation in quantities which have been used to date in the design of non-axisymmetric endwalls.

Endwall design procedure

As indicated by Gregory-Smith[21], due to the complexity of their flows, modern gas turbines require the use of fully viscous, 3-dimensional CFD computations for their aerodynamic design, which can - depending on the density of meshes used for the calculations - be extremely computationally expensive. Further, in order to compare the relative effectiveness of each objective function for the design of endwall contours in this investigation, it was necessary to produce as globally optimal designs as possible. Previous researchers, such as Macpherson[13] & McIntosh[16] used the Genetic Algorithm of Holland[22] to search for the most optimal solution, although their computational meshes were relatively small ($\sim 300 \times 10^3$ cells) and they had access to a large scale cluster computing service. Others, who were less concerned with locating the global optimum, have used various gradient-based algorithms, such as Nagel[9] & Praisner[10] who both used sequential quadratic programming (SQP) to search for improved designs.

In order to produce mesh independent results for the objective function quantities and blade geometries used in this investigation, as well as maximize the fidelity of the predicted results, it was found that much larger meshes ($\sim 2.4 \times 10^6$ cells) were required, which made the use of direct global optimization techniques such as those used mentioned above, computationally intractable

Surrogate modelling and EGO algorithm

In order to minimize the computational costs associated with the objective function evaluations for the current investigation, a design system based on the surrogate-based *EGO* (Efficient Global Optimization) scheme of Jones[23] (which itself is based on the so-called DACE (Design and Analysis of Computer Experiments) metamodel of Sacks[24]) was developed.

Although originally developed as a geostatistical technique for predicting the distribution of mineral deposits by Krige[25], the DACE model has become significantly more widely used basis for surrogate based optimization (SBO) routines, in which some of the original computational expense is alleviated by performing a portion of the required objective function evaluations on so-called 'surrogate' models, whose computational costs are less than those of the original function. Further, some of the reasons for the increased popularity of the DACE model within the engineering community is because of it's inherent ability to model the highly complex and non-linear functions often found in engineering problems without any *a priori* knowledge of the objective function hypersurface being approximated, as well as its ability to make predictions about the accuracy of its own predictions of the original objective function it models[23].

Table 1. Summary of design metrics used to date in the design of non-axisymmetric endwall contours

Researcher	Test geometry	Parametrisation	Design metric (quantity)
Rose[3]	Turbine	Sinusoidal	*static pressure*
Harvey et al[4]	Cascade, 2D	Fourier	*static pressure, yaw angle*
Brennan et al[6]	Turbine	Fourier	$SKEH_B$
Harvey et al[8]	Turbine	Fourier	$SKEH_B$
Praisner et al[10]	Cascade, 2D	Free	$C_{p0}+$ *yaw angle*
Germain et al[11]	Turbine	Sinusoidal	$SKE_C + C_{p0}+$ *yaw angle*
Schuepbach et al[12]	Turbine	Sinusoidal	SKE_C, *yaw angle*
Macpherson et al[13]	Cascade, 2D	Fourier	$C_{ske}+$ *yaw angle*
Poehler et al[14]	Turbine	Sinusoidal	$SKEH_D$
Vazques et al[15]	Cascade, 3D	Unknown	$SKEH_B$
McIntosh et al[16]	Cascade, 2D	Fourier	$C_{ske}, \int u^3 dA$, *yaw angle*
Hilfer et al[17]	Cascade, 2D	Fourier	$C_{ske} + \dot{m}+$ *yaw angle*
Bergh et al[18]	Turbine	Fourier	$C_{ske}+$ *yaw angle*
Miyoshi et al[19]	Turbine	Free	ϵ (enstrophy)
Poehler et al[20]	Turbine	Free	stage efficiency

As shown in Eqn. 1, in contrast to the many other regression models, in which the majority of effort is placed on the selection of the underlying trend model and comparatively little emphasis is placed on any error (or deviation) terms, in the DACE model, the objective function is modelled as a stationary Gaussian process comprising of a relatively simple trend model (a constant process mean) and a series of stochastic but correlated deviations from this mean:-

$$y\left(\vec{x}^p\right) = \underbrace{\hat{\mu}}_{\text{process mean}} + \underbrace{\epsilon(\vec{x}^p)}_{\text{deviation}} \qquad (1)$$

where y is the predicted objective function value, $\hat{\mu}$ is the process mean, ϵ is the deviation term and $\vec{x}^p$ is the current prediction point.

Since, as indicated previously, in the DACE model the majority of effort is concerned with the modelling of the process deviation, the form of the so-called *Spatial Correlation Functions* (SCF) used to model this term are given special attention. Among the most common $SCF's$ are the so-called *exponential correlation functions*, in which the correlation between the deviation terms at two different input locations may be given by Eqn. 2:-

$$Corr\left[\epsilon\left(\vec{x}^i\right), \epsilon\left(\vec{x}^j\right)\right] = exp\left[-d\left(\vec{x}^i, \vec{x}^j\right)\right] \qquad (2)$$

where $d(\vec{x}^i, \vec{x}^j)$ is a *weighted* difference between the ith & j^{th} input vectors.

Further, in the DACE model, the weighted difference may be given Eqn. 3:-

$$d\left(\vec{x}^i, \vec{x}^j\right) = \sum_{h=1}^{k} \theta_h \left|x_h^i - x_h^j\right|^{p_h} \qquad (3)$$

where k is the problem dimensionality (i.e. the length each input vector), θ_h is the weighting applied to the hth vector component difference, x_h^i, x_h^j are the hth component of the ith and j^{th} input vectors and p_h is a smoothness parameter, which for this investigation, was set to 1.9.

As indicated previously, the *EGO* algorithm is a search methodology originally developed by Jones[23] for use with the DACE metamodel and as suggested by its name, was intended for the global optimization of systems

Table 2. *EGO* optimization schedule

Iteration	value	'g' value	Use
1 - 150	EI_1	1	Balanced global/local search
150 - 300	WB_1	0	Local search
$\geq$ 300	WB_1	0	Local search (if required)

incorporating expensive objective functions. Principally, the major advantage of this approach, is its ability to exploit the DACE model's capability to make predictions about the accuracy of its own predictions. Briefly, rather than advancing by attempting to optimize the DACE model objective function predictions directly, the *EGO* algorithm proceeds by selecting candidate input vectors which maximize the so-called *Expected Improvement* (EI) of the underlying DACE model, which takes into account regions of already *known* favourable objective function values as well as regions in the model with a high degree of uncertainty. Following the construction of this surface, appropriate *Infill Search Criteria* (ISC) are used to determine which areas of the EI hypersurface are most likely to yield an improvement in the current best known (true) objective function value, after which the true but expensive objective function is evaluated. By using this approach, the efficiency of the optimization routine is significantly improved, since expensive objective function evaluations are limited to those regions of the parameter space where an improvement in the current best objective function value is most likely.

A combination of ISC were used as part of the *EGO* algorithm for this investigation similar to the so-called *Cool* criterion of Sasena[26], although for the present case, a combination of only two infill criteria were used:- the EI_1 ISC function, in which the searching of the surrogate objective function surface is reasonably balanced between areas of already known low objective function values (and therefore high expected improvement) and areas of the model with reasonably high uncertainty, and the so-called WB_1 criteria, which was developed by Watson & Barnes[27] as a means for determining threshold-bounded extremes, and therefore (in the current context), an extremely local search in regions with already known favourable objective function

Table 3. Driven curve parameters

Curve number	Amplitude (c_n)	Period (n_n)	Phase shift terms (ψ_i)
2_a	$\dfrac{(c_2 + c_3)}{2}$	$\dfrac{(n_2 + n_3)}{2}$	$\dfrac{\sum_{i=1}^{1} \psi_i + \sum_{i=1}^{2} \psi_i}{2}$
3_a	$\dfrac{(c_3 + c_4)}{2}$	$\dfrac{(n_3 + n_4)}{2}$	$\dfrac{\sum_{i=1}^{2} \psi_i + \sum_{i=1}^{3} \psi_i}{2}$
4_a	$\dfrac{(c_4 + c_5)}{2}$	$\dfrac{(n_4 + n_5)}{2}$	$\dfrac{\sum_{i=1}^{3} \psi_i + \sum_{i=1}^{4} \psi_i}{2}$

values. The final *EGO* optimization schedule used in this investigation is given in Table 2. Finally, for a full treatment of the *EGO* and the *Cool* algorithms, the reader is directed to the previous works of Jones and Sasena respectively [23,28].

Endwall parametrisation

In this investigation, the rotor hub endwall was parameterised using a variation of the so-called 'Fourier series' approach of Harvey[4], in which the endwall curvature is defined by a series of curves defined by Eqn. 4 in the circumferential direction and using interpolating non-uniform rational b-splines in the axial direction.

$$\delta r(\theta) = a_0 + \sum_{n=1}^{k} \left(a_n \sin\left(\frac{n\pi\theta}{P}\right) + b_n \cos\left(\frac{n\pi\theta}{P}\right) \right) \tag{4}$$

This approach was used as, even with a relatively small number of harmonics ($k = 3$) included in the definition of each circumferential endwall curve, a considerably large range of endwall geometries could be produced. In addition, as a result of the periodic nature of the expression, this parametrisation helped to preserve the overall area of the flow passage and so limited the effects of so-called *throat errors* in the final designs produced in that investigation.

One issue encountered by almost all researchers who used the parametrisation of Eqn. 4, was that the endwall curvature it produced was *too* complex. As a result, in most investigations, the number of harmonics included in the definition of the endwall curvature, was limited to 1.

Since in this investigation, the main objective was to test the efficacy of each flow metric in terms of its fundamental ability to isolate and then target the secondary flows, the above parametrisation was simplified to one equivalent to the inclusion of only the first harmonic of Eqn. 4 and is given in Eqn. 5 below. A further advantage of this parametrisation, was that this formulation reduced the epistatis of the endwall parameters, allowing the endwall amplitude, periodicity & phase angles to be controlled directly rather than as a result of a combination of the coefficients a_n & b_n for each harmonic. This in turn then also allowed for the simpler imposition of the variable constraints required for each optimization run.

$$r_k(\theta) = R_0 + c_k \sin\left(\frac{n_k \pi \theta}{P} + \left(\psi_1 + \sum_{i=2}^{k,k \neq 1} \varphi_i\right)\right) \tag{5}$$
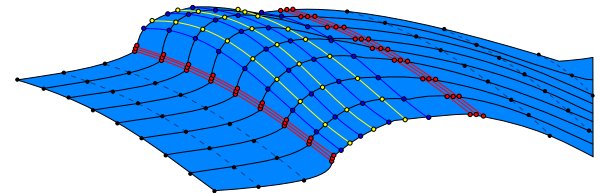
The parametrisation of Eqn. 5 was applied to the endwall surface as a set of $\times 4$ 'driving' curves in the circumferential direction (Fig. 3, curves $2/3/4/5$). In addition, a set of $\times 9$ *NURBS* curves were used to specify the curvature of the
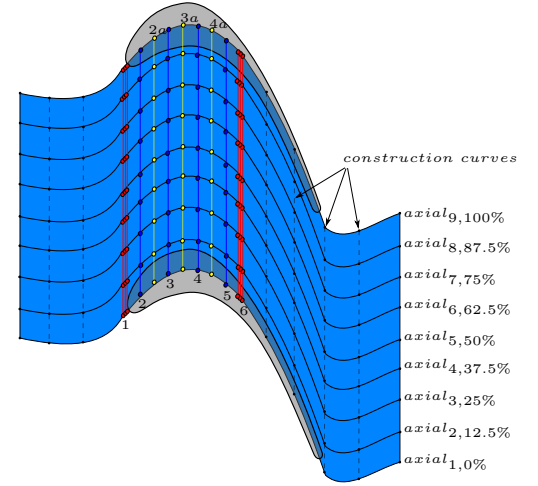
(a) Overview
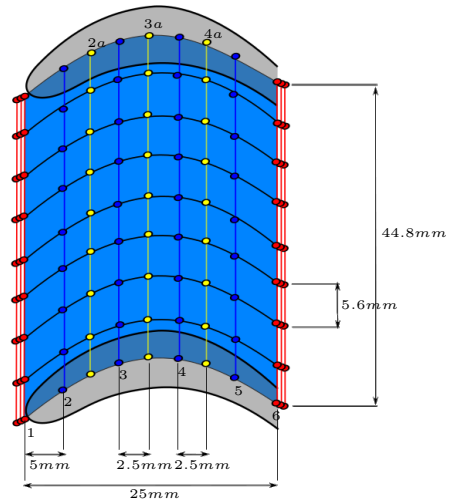
(b) Dimensions

(c) Perspective

Figure 3. Curve network used to generate the rotor non-axisymmetric endwall surface. The circumferential curvature defined by the *driving* (2, 3, 4 & 5) & *driven* ($2a$, $3a$ & $4a$) curves. The axial curvature was defined by the *NURBS* curves ($axial_{1-9}$) fitted through control points at 12.5% intervals along each circumferential curve. The limiting annular curves (1 & 6) and construction curves are also shown

Table 4. Variable constraints used with the turbine endwall parametrisation

Variable		Constraint
Endwall amplitude	c_k	$0 \leq c_k \leq 3.5mm$
Endwall amplitude change	$\Delta c_{k,k+1}$	$0 \leq \Delta c_{k,k+1} \leq 2mm$
Curve periodicity	n_k	$0.5 \leq n_k \leq 1$
Periodicity	$\Delta n_{k,k+1}$	$0 \leq \Delta n_{k,k+1} \leq 0.25$
Phase angle (curve 1)	ψ_1	$-180° \leq \psi_1 \leq 180°$
Phase angle change (curve 2/3/4)	φ_i	$-45° \leq \varphi_i \leq 45°$

endwall in the geometry in the axial direction. *NURBS* curves were selected because of their more local responsiveness to perturbations in their control points and this was considered beneficial for this case. In addition however, in order to ensure a smooth transition between each of the 'driving' curves, an additional ×3 'driven' curves (Fig. 3, curves 2a/3a/4a) were used with the coefficients of these curves calculated as per Table 3. Thereafter, a series of ×3 annular curves were used at the entrance and exit of the contoured region to constrain the endwall to the datum endwall radius ahead and aft of the blade passage.

Finally, as shown in Fig. 3a, the endwall design space was limited to the forward portion of the blade passage. This was done for two reasons:- firstly, since this investigation considered a rotor in an actual rotating albeit model turbine, it was required that the contouring be limited to a region which did not extend far up or downstream of the rotating blade row, and secondly, a series of investigations into various endwall designs at Durham University, showed that, of all the designs produced, the most successful of these was the so-called Durham *P2* design[1], whose contouring was limited to a reasonably compact portion of the endwall close to the leading edge of the blade and therefore a similar approach was taken during the design of the present endwall parametrisation scheme.

Constraints Despite the positive nature of the pressure gradients in a turbine blade row and because of the three-dimensional nature of endwall contouring, thus far one of the main issues encountered has been the introduction of excessive local diffusion into the flow, which can lead to flow separations and high total pressure losses, nullifying any benefits introduced as a result of the endwall contouring. In order to minimize this, in addition to the use of various boundary constraints on the design vector parameters, the change between the endwall parameters of successive 'driving' curves were also limited. For instance, in addition to limiting the maximum and minimum amplitudes of each driving curve, the change in amplitude between each curve was also limited. A full summary of the variable constraints used for all designs are summarized in Table 4.

Database design

The initial DACE model databases were constructed by constructing a Latin Hypercube Sampling (*LHS*) design on the unit hypercube using the MATLAB *lhsdesign.m* function which was then further optimized using the *maximin* optimization criteria. Because the *maximin* criteria is a relatively difficult criteria to optimize, the total number of iterations for the *LHS* optimizations were set at $500 \times n_{parameters}$. The size of the databases were selected using

Table 5. Optimizer settings for the *MLE* and *ISC* subproblems

Setting	Value
Population size (*popsize*)	48
Scaling factor (F)	0.8
Cross-over rate (Cr)	0.8
$Var_{hi/lo}$ (*MLE*)	10^2 / 10^{-12}
$Var_{hi/lo}$ (*ISC*)	as per Table 4
Min / Max iterations ($it_{min/max}$) (*MLE*)	- / 3500
Min / Max iterations ($it_{min/max}$) (*ISC*)	1000 / 5000

the $n_{samples} = n_{parameters} \times 10$ rule-of-thumb resulting in a total of 120 initial designs for each optimization quantity. Finite volume (*FV*) meshes for each database design were then constructed and numerical solutions produced for each geometry. For each mesh, a minimum element skewness of 0.3 was tolerated while each simulation was converged until the each of the residuals was decreased to a minimum of than 1×10^{-5} and in most cases, below 1×10^{-6}. Mesh skewness and residuals were calculated using the definitions presented in [29] & [30] respectively.

Any geometry for which a *FV* mesh of appropriate quality or for which a satisfactorily converged steady-state solution could not be computed was removed from their respective model databases. Although this removal of these designs from the database meant that the remaining databases were not strictly complete *LHS* designs anymore, because only a few designs were actually removed (~ 10) from the databases, this was considered acceptable.

Fitting

While a number of methods exist for the fitting of DACE models, the so-called *Maximum Likelihood Estimation* (*MLE*) method in which the so-called *likelihood function* ($\mathcal{L}$) or *concentrated likelihood function* ($\mathcal{L}_c$) is maximized, was chosen for this work. Briefly, in contrast to the generating random variables from a *known* distribution, the *MLE* approach seeks to determine the hyperparameters $\vec{\theta}$ of an assumed statistical model such that the likelihood of the observed variables having been drawn from that distribution, is maximized. Since in the DACE method, the deviations of the model from the mean are modelled as random stochastic deviations from the process mean, this approach has been found to be a robust choice for the estimation of the requisite model hyperparameters[31]. While it is possible in some circumstances for closed form solutions for the optimum model parameters to be found, in most cases, the optimal model parameters must be determined using some numerical optimization technique. In addition, in practice, in order to avoid issues related to the large 'flat' zero gradient portions and ridges often found on the likelihood surface (which then

may present difficulties to the chosen optimization approach) as well as because this does not change the location of the maximum likelihood estimate, in most cases, the logarithm of the concentrated likelihood function $(\ln(\mathcal{L}_c))$ is used as the target objective function during the MLE procedure.

Following Jones[23], $\ln(\mathcal{L}_c)$ can be expressed by Eqn. 6:-

$$\ln\left(\mathcal{L}_c\left(\vec{\theta}\right)\right) = -\frac{n\ln\left(\sigma^2\right) + \ln\left(|\mathbf{R}|\right)}{2} \qquad (6)$$

where σ^2 is the variance of the DACE model deviations, n is the number of data points in the sample, and $\mathbf{R}$ is a matrix of correlations between the known data points (i.e. the correlation matrix), where $(R_{i,j}) = Corr\left[\epsilon\left(\vec{x}^i\right), \epsilon\left(\vec{x}^j\right)\right]$.

In this investigation, the MLE problem was posed as a minimization problem, and therefore finally, the model parameter estimation problem was given by:-

$$\min_{\vec{\theta} \in \mathbb{R}^k} : -\ln\left(\mathcal{L}_c\left(\vec{\theta}\right)\right) \qquad (7)$$

subject to:-

$$\theta_h > 0$$

where:-

$$h = 1, 2, ..., k$$

Two population-based, evolutionary algorithms were trialled for the solution of the MLE subproblem:- the well-known Genetic Algorithm (GA) of Holland[22] and the relatively new Differential Evolution (DE) algorithm of Storn and Price[32]. Testing on three sets of CFD generated aerodynamic data showed that with the exception of one dataset, the DE algorithm was found to converge to not only better (i.e. higher) optima but also faster and more consistently to these maximum points. It should be noted that, although, as was expected, as a result of the generally higher MLE estimates produced by the DE routine, the Root Mean Square errors for the DE-fitted DACE models were lower, in general, smaller Maximum Error values were produced by the GA-fitted DACE models. The final settings for both the MLE and ISC subproblems are summarized in Table 5.

A number of well-known issues exist with the use of the MLE approach for model fitting. In this investigation, the two main issues encountered were:- the first associated with the maximization of the $\ln(\mathcal{L}_c)$ function and the second related to the numerical issues associated with the ill-conditioning of the correlation matrix ($\mathbf{R}$) which is used to store the correlation data between various data points in the DACE model database.

Remedies to MLE optimization problem Depending on the arrangement of the datapoints used in the construction of the initial DACE model database, it is possible that the $\ln(\mathcal{L}_c)$ function may be found to be either monotonically increasing or decreasing with increasing or decreasing magnitudes of the model hyperparameters, and therefore contain no internal optimizers. In these cases, the MLE fitting routine will either select as small or as large as possible a value of the hyperparameters. In the case were the $\ln(\mathcal{L}_c)$ function is found to increase with decreasing values of the hyperparameters (and therefore very small values for $\vec{\theta}$ are selected), numerical issues related to the

poor conditioning of the correlation matrix $\mathbf{R}$ are usually encountered, while very large values for the components of $\vec{\theta}$ usually result in the degradation of the predicted DACE model hypersurface to that of a constant trend punctuated at the location of each data point by a local excursion to the known data point value, leading to very poor generalisation of the model between each known data point.

In order to deal with this situation, in addition to variable constraints on the maximum and minimum $\vec{\theta}$ parameters, simple inequality constraints were used to limit the maximum value of the $\ln(\mathcal{L}_c)$ function. In addition, a further inequality constraint was used to prevent the condition number (κ) of the correlation matrix $\mathbf{R}$ getting too small.

$$c_1(\vec{\theta}) : \ln(\mathcal{L}_c) \geq -1 \times 10^{15} \qquad (8)$$
$$c_2(\vec{\theta}) : \ln(\mathcal{L}_c) \leq 1 \times 10^{15} \qquad (9)$$
$$c_3(\vec{\theta}) : \kappa(\tilde{\mathbf{R}}) \leq 1 \times 10^{13} \qquad (10)$$
$$b_1 : \vec{\theta} \leq 10^2 \qquad (11)$$
$$b_2 : \vec{\theta} \geq 10^{-12} \qquad (12)$$

where $\tilde{\mathbf{R}}$ is the *regularized* correlation matrix(see following section), $\kappa(\tilde{\mathbf{R}}) = \frac{|\lambda|_{max}}{|\lambda|_{min}}$, $\tilde{\mathbf{R}} \in \mathbb{R}^{m \times m}$ and λ_{max} and λ_{min} are the largest and smallest eigenvalues of $\tilde{\mathbf{R}}$ respectively.

Remedies to ill-conditioning of correlation matrix $\mathbf{R}$ The ill-conditioning of the DACE model correlation matrix $\mathbf{R}$ is a serious issue related to the use of the DACE model as well as EGO algorithm because the numerical inversion of the matrix is required at a number of junctures throughout the model fitting and prediction procedures.

As indicated previously, the distances between the data points are computed using a *weighted* distance and where the weightings applied to each dimension correspond to the components of the $\vec{\theta}$ hyperparameter vector (optimized during the MLE fitting procedure above). Following Kok[33], an alternative form for this weighted distance is given in Eqn. 13, where b_h is a *range parameter* equal to $1/\theta_h$ and all other quantities are as defined previously.

$$d\left(\vec{x}^i, \vec{x}^j\right) = \sum_{h=1}^{k} \left|\frac{x_h^i - x_h^j}{b_h}\right|^{P_h} \qquad (13)$$

Since, as discussed above, the condition number (κ) of a matrix is given by the ratio of *maximum : minimum* eigenvalues of $\mathbf{R}$, from Eqn. 13, it is clear that as $\theta_h \to 0$, $b_h \to \infty$ and the corresponding weighted distances between the data points becomes infinitely small. Under these conditions, $\mathbf{R}$ tends towards the *unit* matrix, all of whose eigenvalues are equivalent to 0, apart from one, which is equal to the number of data points in the database. In this case, the condition of $\mathbf{R}$ will decrease since $\kappa(\mathbf{R}) \to \infty$.

Physically, the decrease in the weighted distances between each data point with the decreasing $\vec{\theta}$ hyperparameters may be viewed as the data points used in the correlation matrix becoming increasingly close together until the columns of $\mathbf{R}$ become linearly dependent and offer no correlation information to the underlying DACE model.

A second scenario, although unrelated to the above, but which also has the same effect, is that which is potentially approached at the end of an EGO optimization run, and that is the repeated sampling of the modelled objective function in an increasingly small region of the parameter space. This also results in a decrease in the linear independence of the columns of $\mathbf{R}$ and therefore its condition number.

In order to reduce the effects of these two scenarios, the method of Lophaven[34] was used, in which a regularized correlation matrix $\tilde{\mathbf{R}}$ is defined by adding a small positive number (ν) (the so-called *nugget*) to the diagonal of $\mathbf{R}$. Following Lophaven[34], the addition of the nugget to the unmodified correlation matrix is guaranteed to improve the conditioning of $\mathbf{R}$ because since $\tilde{\lambda}_j = \lambda_j + \nu$, the condition of $\kappa(\tilde{\mathbf{R}}) \underset{always}{<} \kappa(\mathbf{R})$ since $\left(\frac{|\lambda|_{max}+\nu}{|\lambda|_{min}+\nu} \right) \underset{always}{<} \left(\frac{|\lambda|_{max}}{|\lambda|_{min}} \right)$.

For this investigation, the nugget was set to:-

$$\nu = (10 + m)\epsilon_m \tag{14}$$

where m was the number of initial data points in the DACE model database and ϵ_m was the so-called machine accuracy equivalent to $\sim 2.2204e^{-16}$.

Model fitting validation Using the techniques above, separate DACE models were generated for each of the target quantities which were to be used as the basis of the objective functions for each endwall. After fitting, the quality of each fit was assessed using the so-called *Leave-One-Out* (LOO) cross-validation technique, in which the optimum $\vec{\theta}$ hyperparameters are estimated, and thereafter a single database sample is removed from the database, and the various DACE model parameters (i.e. $\mathbf{R}$) are re-calculated, and then the value of the removed sample is estimated using the original $\vec{\theta}$ hyperparameters and the reduced model coefficients. This estimated value is then compared with the original known value of the removed sample.

For each database, the LOO cross-validations were performed for each of the database entries, whereafter the validity of each database was assessed by computing the following metrics:- *Root Mean Square error* ($RMSE$), *Max error*, and *Max Std Residual* (R_{std}). The consolidated results for each initial database are shown in Table 6 and while the root mean square and max errors should be low, in addition, since the DACE model should be 99.7% sure of its predictions, the maximum standard residual for each database should be lie within 3-standard deviations of the mean. While this was acheived for most of the metrics, the maximum residual for the η_{de} database did not meet this criteria, however, despite this shortcoming, this database was deemed acceptable since the criteria was only slightly breached.

Stopping criteria

The use of the population-based DE algorithm for the fitting of the DACE model hyperparameters, combined with the computational expense associated with the calculation of the concentrated $\ln(\mathcal{L}_c)$ function for the MLE sub-optimization problem, meant that - as the number of EGO algorithm iterations increased - the overall computational expense associated with the use of the DACE model increased. This
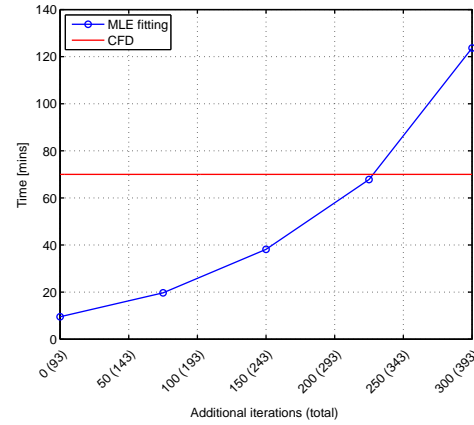
Figure 4. Comparison of time requirements for DACE model parameter tuning with database size

is because at the end of each EGO iteration, the results of the previous objective function evaluation are added to the DACE model database, which in turn results in an increase in the overall size of the correlation matrix, which must be numerically inverted during each $\ln(\mathcal{L}_c)$ function evaluation.

Since, in many cases, the increase in the temporal requirements associated with the fitting of the DACE model may approach or even exceed those of the CFD model calculations, in many cases, a stopping criteria based on the maximum number of EGO iterations which can be reasonably performed is used instead of running the algorithm to some sort of predetermined convergence criteria.

For this investigation, the CFD calculations were performed using a 64-core, multithreaded compute server. The walltime requirements for the MLE fitting vs. CFD computations for the total number of EGO iterations, as well as the total DACE model database and total predicted optimization time for a single endwall design, are shown in Fig. 4. Based on the overall total optimization times shown in Fig. 4, a total number of 300 EGO iterations was selected for each design optimization. This corresponded to a model fitting time requirement equivalent to nearly $1^3/4$ times ($\sim$ 123 min) that of the actual CFD computations ($\sim$ 70 min), and a predicted total optimization time requirement of ~ 24 days per design.

Test case

The test case used in this investigation was the CSIR low speed, $1^1/2$ stage research turbine. At the hub, the blading of the rotor and 2nd stage nozzle for this turbine closely resembles that of the Rolls-Royce RB211 high pressure turbine, although modifications to the aerofoil and twist of the blades were made to accommodate the specific details of the current environment. In this investigation, the turbine was used in its $1-$stage configuration, with the downstream (i.e. $S2$) nozzle removed. This was to allow for quasi-'mixed-out' measurements some distance downstream of the rotor in addition to at the rotor exit, to be made.

A summary of the design and working characteristics of the turbine are shown in Table 7, where the large turning

Table 6. Comparison of *LOO* cross-validated *RMSE*, *Max Error* & *Max* R_{std} values for each objective function for the initial DACE model database

Objective function	$n_{\mathrm{points,final}}$	Leave-One-Out cross-validation			
		Mean	RMSE	Max Error	Max R_{std}
η_{tt}-based	93	20.52	0.55% (0.11)	1.38% (0.28)	2.43
C_{ske}-based	93	10.61	5.39% (0.57)	16.04% (1.70)	2.37
$C_{p0,rel}$-based	92	14.92	1.36% (0.20)	4.10% (0.61)	2.74
β_{dev}-based	93	5.02	4.08% (0.20)	13.13% (0.65)	2.82
$SKEH$-based	93	28.58	7.81% (2.23)	22.37% (6.39)	2.68
η_{de}-based	93	4.41	5.36% (0.23)	15.22% (0.67)	3.06
$C_{ske,1} + \beta_{dev,0.7}$-based	93	14.09	5.04% (0.71)	15.93% (2.24)	2.53
$C_{p0,rel,1} + \beta_{dev,0.7}$-based	92	18.40	1.25% (0.23)	2.50% (0.46)	2.60

Table 7. Summary of turbine specifications

INLET		
Design axial velocity		21.38 m/s
Design wheel speed		2300
NGV		
No. of blades		30
Inlet angle	Hub	0°
	Tip	0°
Outlet angle	Hub	68.26°
	Tip	61.20°
ROTOR		
No. of blades		20
Inlet angle	Hub	42.75°
	Tip	-23.98°
Outlet angle	Hub	-68.00°
	Tip	-71.15°
Stage power		3.87kW
Stage pressure ratio		1.0393
Exit Reynolds number		127,500
Flow coefficient (ϕ_{hub})		0.52
Loading coefficient (ψ_{hub})		2.94
Degree of reaction (Λ_{hub})		0.38

angle ($\sim 111°$) for the rotor is clear, in turn making this case a good candidate for studies involving secondary flows.

Numerical modelling

The numerical model used in this investigation was limited to the portion of the turbine downstream of the *NGV* blade row. This was done in order to reduce the computational expense related to evaluation of the true objective function during each *EGO* iteration. Accordingly, the flow into the rotor domain was modelled using 1-dimensional profiles for the flow and turbulence quantities and were extracted from a previous simulation of the full turbine in which the well-known mixing plane approach was used to link the stationary and rotating domains. In this approach, the transported quantities are assumed to be 'mixed out', meaning that the upstream variables are circumferentially averaged in the radial direction (for an axial machine), and then applied as a 1-dimensional profile to the inlet of the downstream domain. Other quantities, such as the fluid pressure, which is specified at the outlet of the turbine, are averaged at the inlet boundary to the downstream domain, and propagated into the upstream domain. Therefore, the use of radial profiles

in place of the upstream blade row was identically similar to the mixing plane approach, except that changes in the downstream pressure field are *not* propagated back upstream where they may affect the flow in the *NGV* blade row. However, since the potential effects of the downstream blade (i.e. the rotor) on the upstream blade row where seen to be negligible, this simplification was deemed to be acceptable.

Geometry generation and meshing The turbine endwall geometry for each CFD calculation was generated using the Gambit software application, which although is primarily intended as a meshing application, was used only for the generation of the endwall geometry in this investigation. This was done by importing the circumferential driving and driven curve definitions into the application as formatted point data and generating the following network curves discussed previously, and then generating the 3-dimensional endwall surface. The endwall surface was then imported into the ICEMCFD meshing software suite, where the remaining turbine geometry was generated.

In order to ensure as much uniformity as possible between different designs, a single prototype CFD mesh definition was created using the annular turbine case, and the endwall portions of this mesh then mapped onto the perturbed geometry of each candidate endwall, and the perturbed mesh definition then exported to the CFD solver. The veracity of this approach was confirmed by using the same mesh definition discussed above to predict the flow for an existing non-axisymmetric endwall design, for which existing experimental results were also available. Finally, a mesh independence study using both the datum (annular) as well as the existing contoured endwall design was carried out and the mesh independence of the prototype mesh confirmed by examining the mass-averaged metrics defined previously for both cases. A summary of the final prototype mesh specifications is given in Table 8.

In order to maximize the fidelity of the CFD calculations, the prototype mesh was created to be as dense as possible without rendering the overall optimization procedure computationally intractable. This included the full resolution of the flow boundary layers on both the endwall as well as blade surfaces and the flow in the tip gap, which is often modelled using periodic boundaries to reduce computational expense.

Computational Fluid Dynamics The flow solutions for each *EGO* iteration were computed using the Ansys Fluent CFD solver, which was selected as a result of its ability to use

Table 8. Summary of final optimization mesh specifications

Parameter	Value
Total cell count	$\sim 2.4M$
Radial	108
Circumferential	38
Boundary layer cells	
Blade	20
Endwall	20
Tip gap	25
Near wall Re Number (y^+) (endwall)	
Avg	0.497
Min	0.004
Max	0.564

(a) Overview

(b) Leading edge detail (hub)

(c) Trailing edge detail (hub)

Figure 5. Computational mesh used in CFD calculations showing the overall rotor configuration, hub leading and trailing edge detail (Rotor suction surface not shown).

to the so-called coupled-solver, in which the discretized pressure correction and momentum equations are solved in a coupled fashion rather than sequentially, often leading to faster convergence.

Because the endwall design routine was designed to run without user intervention, the under-relaxation factors for each equation were set to reasonably conservative values which were selected by trial and error to provide as stable convergence as possible but without affecting the overall solution time too adversely.

The turbulent effects of the flow were modelled using the $k - \omega\ SST$ turbulence closure of Menter[35], which is 2-equation, eddy-viscosity model. During the development of the model, a number of alternative turbulence closures were trialled, included the 7-equation, second order Reynolds Stress Model (RSM), in which the anisotropy of the turbulent eddies are considered, as well as a transition sensitized version of the $k - \omega\ SST$ model using the γ-transition revision of Menter[36]. Despite the additional fidelity of both the RSM and γ-transition models, no significant improvements in terms of either the flow (velocity or angle) or optimization quantities (coefficient of loss / secondary kinetic energy) were noted. In addition, in comparison to a number of similar 2-equation models, of those models which were found to adequately predict the flow, the $k - \omega\ SST$ was found to be more sensitive to changes in the endwall geometries, and therefore considered a better candidate for use as part of an optimization routine.
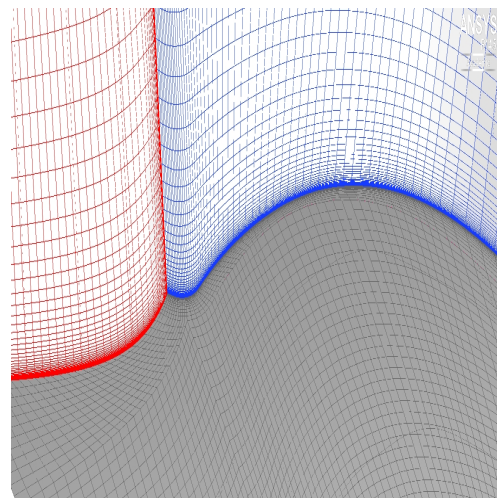
Objective functions

Eight different objective functions were trialled during this investigation:- including 6 'simple' (which comprised of only a single metric) and 2 'compound' (which comprised of a combination of two different base metrics). In all cases, the problem at hand was formulated as a minimization problem, while for the 'compound' functions, the multi-objective nature of the problems were converted to equivalent single objective optimizations by constructing a weighted *pseudo*-objective function. Further, for the 'compound' objective functions, the weightings for each metric was selected from the similar examples in the literature.
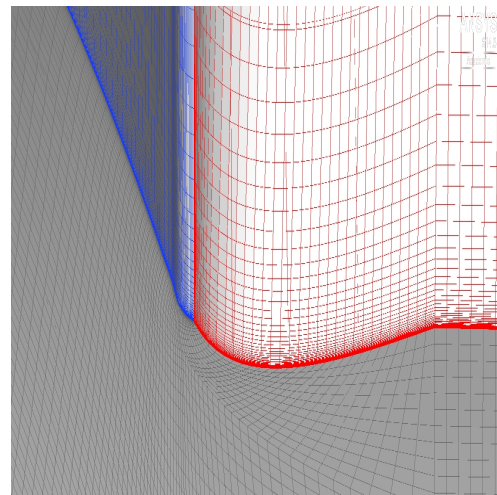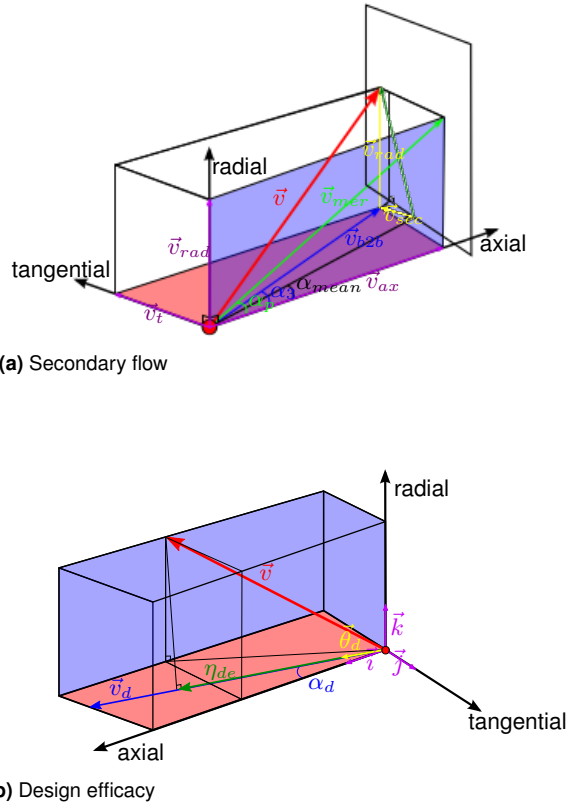
For the efficiency (i.e. η_{tt}, Eqn. 15)-based objective function, the rotor efficiency was defined as the well-known rotor total-total efficiency, while for the secondary kinetic energy (i.e. C_{ske}, Eqn. 16)- and design efficacy (i.e. η_{de}, Eqn. 20)-based objective functions, the flow vectors involved in the definition of each metric are shown in Fig. 6a & 6b respectively. The rotor loss ($C_{p0,rel}$, Eqn. 17)-based objective function was formulated as the loss in total pressure between the inlet and outlet of the rotor

(a) Secondary flow

(b) Design efficacy

Figure 6. Definition of flow vectors for the C_{ske} and η_{de} metrics

blade passage which is identical to the well-known loss coefficient used widely for turbomachinery design, although for the present case, since the blade row in question was a *rotating* blade row, the loss in total *relative* pressure between the inlet and outlet was used. Finally, the flow deviation from design (β_{dev}, Eqn. 18)- and secondary kinetic energy helicity ($SKEH$, Eqn. 19)-based objective functions were calculated at the simple difference between the local design and actual flow angle and the dot product of the secondary kinetic energy and streamwise helicity.

Efficiency

$$\eta_{tt} = \frac{w}{(p_{02} - p_{3,is})/\rho - 1/2 V_{3,is}^2} \quad (15)$$

Secondary kinetic energy

$$C_{ske} = \frac{V_{3,sec}^2 + V_{3,rad}^2}{V_2^2} \quad (16)$$

Loss

$$C_{p0,rel} = \frac{p_{02,rel} - p_{03,rel}}{p_{03,rel,mean} - p_{3,mean}} \quad (17)$$

Flow deviation

$$\beta_{dev}(S) = |\beta_3(S) - \beta_{3,d}(S)| \quad (18)$$

Secondary kinetic energy helicity

$$SKEH = (SKE) \cdot H \quad (19)$$

Design efficacy

$$\eta_{de} = \frac{\vec{v}_3 \cdot \vec{\theta}_{3,d}}{V_{3,d,max}} \quad (20)$$

Table 9. Summary of cost functions

Endwall	Cost function
η_{tt}-based	$(1 - \eta_{tt}) \times 100$
C_{ske}-based	$(1 \times C_{ske}) \times 100$
$C_{p0,rel}$-based	$(1 \times C_{p0,rel}) \times 100$
β_{dev}-based	$(1 \times (\beta_{dev}) \times 1$
$SKEH$-based	$1 \times (SKEH) \div 1 \times 10^5$
η_{de}-based	$1 \times (|1 - \eta_{de}|) \times 100$
$C_{ske,1} + \beta_{dev,0.7}$-based	$(1 \times C_{ske}) + (0.7 \times \beta_{dev}) \times 1$
$C_{p0,rel,1} + \beta_{dev,0.7}$-based	$(1 \times C_{p0,rel}) + (0.7 \times \beta_{dev}) \times 1$

where ρ, p, V and β are the fluid density, pressure, absolute velocity and relative angle magnitudes respectively, w is the rotor specific work, S is the blade span, H is the streamwise helicity, $\vec{v}$ and $\vec{\theta}$ are the flow velocity and angle vectors, and subscripts 02/03, 2/3, *rel*, *d*, *sec* and *rad* denote stagnation, static, relative, design, secondary and radial quantities of the flow at the X2 & X3 measurement planes respectively.

For the $SKEH$, the secondary kinetic energy (SKE) was calculated identically to the C_{ske} except not non-dimensionalized by the upstream kinetic energy.

The rotor efficiency defined in Eqn. 15 represents the aerodynamic performance of the rotor based on incompressible and isentropic assumptions (i.e. flow pressures and velocities only). This was considered acceptable for the current work due to the low speed nature of the rig, and for a full derivation of the quantity the reader is directed to Snedden[2,37]. In addition, and also due to the low pressure nature of the rig, the radial velocities ($V_{3,rad}^2$) in Eqn. 16 where taken to be *any* radial component in the flow, since the design velocity contained *no* radial component. Further, for both the C_{ske} (Eqn. 16) and β_{dev} (Eqn. 18) quantities, the off axis flow velocity and angle were calculated using the design flow angle, which itself was calculated during the design of the blading using the NREC design suite[38] and represented as a function of the blade span (S).

The complete definitions of each objective function are given in Table 9. Finally, where required, a scaling factor was applied to each objective function to ensure that the overall value of each objective function were similar in magnitude for comparative purposes.

Mass-averaging

In those cases where a single input quantity was required for the calculation of the metrics above, the data on each of the X2 & X3 measurement planes were first mass-averaged. This was achieved using the following function:-

$$\overline{Y} = \frac{\sum_i \sum_j Y_{i,j} C_{\dot{m}_{i,j}}}{\sum_i \sum_j C_{\dot{m}_{i,j}}} \quad (21)$$

where $Y_{i,j}$ is the quantity to be averaged, at the i,j^{th} measurement point, $C_{\dot{m}_{i,j}}$ is the mass flow coefficient calculated for the same measurement point, and $\overline{Y}$ is the final mass-averaged quantity. The mass flow coefficient itself ($C_{\dot{m}}$) was calculated using:-

$$C_{\dot{m}_{i,j}} = \frac{\dot{m}_{i,j}}{\dot{m}_{ref_{i,j}}} \quad (22)$$

where $\dot{m}_{i,j}$ is the mass flow at the particular measurement point and $\dot{m}_{ref_{i,j}}$ is a *reference* mass flow based on the turbine inlet flow velocity.

Results

Endwall geometries, cost function reduction and convergence

The final endwall geometries for each of the objective functions are shown in Figs. 7 - 8, while the overall reduction in each cost function, normalized by the starting objective function values, is shown in Fig. 9.

Finally, a collection of statistics, designed to quantify the convergence behaviour of each objective function, are shown in Figs. 10a - 10d. These convergence properties are important, because highly effective (i.e. objective functions resulting in large reductions in objective functions, and therefore potentially large improvements in turbine performance) as well as 'well-behaved' objective functions would be much more attractive to designers.

Endwall geometry In general, and as might be expected, the majority of the so-called 'simple' design metrics produced reasonably simple endwall geometries, with the η_{tt}-, C_{ske}- and β_{dev}-based objective functions producing designs with of a single 'hump-and-dip' type configuration and which - notably - were somewhat similar to previous non-axisymmetric endwall designs produced by other researchers, but using either manual or semi-automated approaches. Further, the simple $C_{p0,rel}$-based design was also noted to produce a somewhat simple geometry, although this was noted to depart somewhat significantly from the classical 'hump-and-dip' configuration noted for the previous 3 designs. Finally, although also 'simple' metrics, the shape of the remaining $SKEH$- and η_{de}-based designs were notably more complex.

When compared with Fig. 9, a similar trend was noticed, and that was that - those metrics that resulted in reasonably well-defined and simple geometries, tended to display reasonably well-behaved convergence properties, with the η_{tt}-, C_{ske}-, β_{dev}- and $C_{p0,rel}$-based designs all tending to show large decreases in their respective cost function magnitudes early on during each optimization run, followed by small, but reasonably regular reductions in the latter phase of each run. This was considered significant because, as indicated previously, cost functions which show predictable but consistent convergence properties are likely to be favoured by designers, especially if large reductions in the overall cost function magnitude can also be achieved.

Significantly, the more complex endwall geometries produced by the $SKEH$- and C_{ske}-based designs were also noted to be associated with poorer convergence characteristics, with Fig. 9 showing that large reductions were still noted for the $SKEH$-based design, even at the end of the final phase of the optimization procedure.
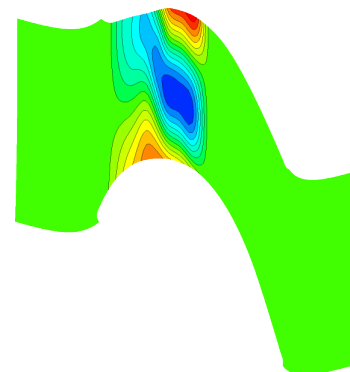
As might be expected, the geometries produced by the 'compound'- design metrics were noticeably more complex than their 'simple' counterparts, although both designs appeared to converge in a reasonably predictable manner. In addition to this, one point of interest associated with the $C_{ske,1} + \beta_{dev,0.7}$-based design, was that, the series of
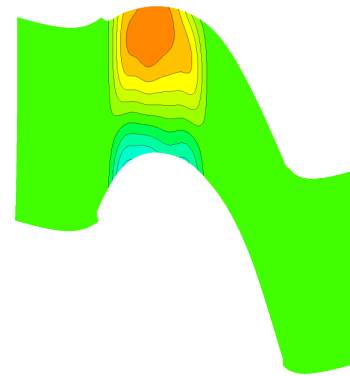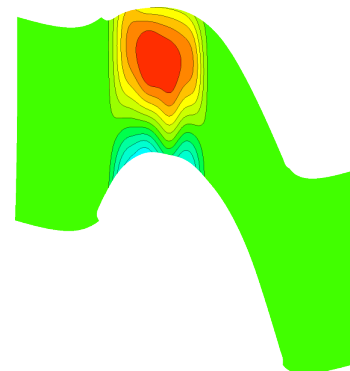

(a) η_{tt}-based
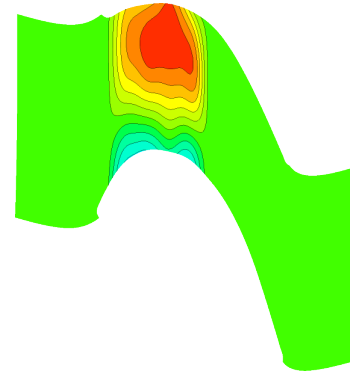

(b) C_{ske}-based


(c) $C_{p0,rel}$-based

(d) β_{dev}-based

reasonably significant reductions in the overall cost function late in the final phase of the overall optimization run, were found to be associated with the formation of the large ridge extending across the blade passage towards to the exit of the contoured portion of the blade passage. Study of the flow in the intermediary designs of this portion of the optimization

Table 10. Summary of DACE and CFD predicted objective function values

Cost function	Final point		$\Delta_{DACE/\mathbf{CFD}}$
	DACE	*CFD*	
η_{tt}-based	19.9010	19.8990	$+0.01\%$ ($+0.0020$)
C_{ske}-based	7.7403	7.7410	-0.01% (-0.0007)
$C_{p0,rel}$-based	13.0840	13.0853	-0.01% (-0.0013)
β_{dev}-based	3.6412	3.6410	$+0.01\%$ ($+0.0002$)
$SKEH$-based	21.9793	21.3741	$+2.83\%$ ($+0.6052$)
η_{de}-based	3.6318	3.6176	$+0.39\%$ ($+0.0142$)
$C_{ske,1} + \beta_{dev,0.7}$-based	10.4587	10.4587	$\sim 0.00\%$ (~ 0.0000)
$C_{p0,rel,1} + \beta_{dev,0.7}$-based	16.1891	16.1890	$\sim 0.00\%$ ($+0.0001$)
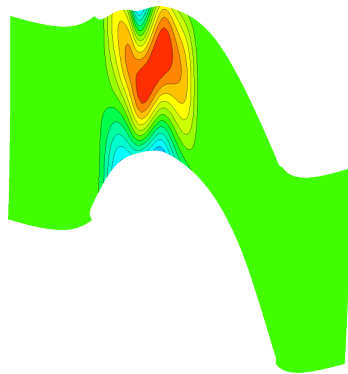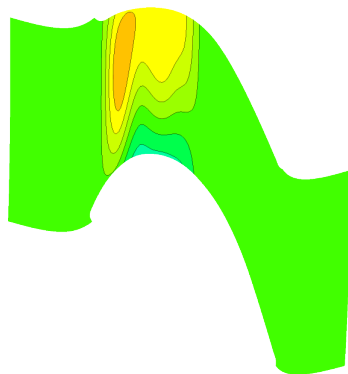
(e) $SKEH$-based
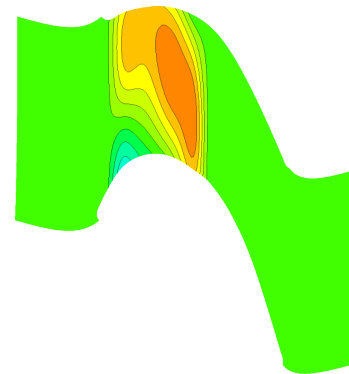
(a) $C_{ske,1} + \beta_{dev,0.7}$-based

(f) η_{de}-based
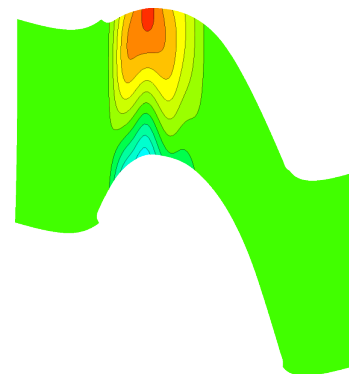
(b) $C_{p0,rel,1} + \beta_{dev,0.7}$-based

Figure 7. 'Simple' designs

Figure 8. 'Compound' designs

run showed that the formation of this ridge, as well as the late reduction in the overall cost function were associated with a large decrease in the flow deviation from design (i.e. β_{dev}) and therefore in this component of the compound metric and therefore, a dominance of this constituent of the compound metric in the final design.

One final observation, in relation to the convergence characteristics of each of the cost function formulations, was that, all those functions which included (in at least one of the components) a 'loss' or 'loss-based' metric (such as the η_{tt}-, $C_{p0,rel}$- and $C_{p0,rel,1} + \beta_{dev,0.7}$-based objective functions), showed the most favourable convergence behaviour, with large early reductions in the cost function, accompanied by small additional (if any) further reductions in the latter part of the optimization procedure, suggesting that potentially large, well-defined regions of low cost function magnitude were present on the objective function hypersurface, and that these were readily discoverable by the design system. In contrast,

those metrics based completely, or at least in part, on the flow angles and / or velocities, showed generally more haphazard convergence behaviour and greater overall sensitivities to the progressive changes in the endwall geometries as manifest by the intermediate endwall designs.

Metamodel performance

The final calculated objective function values for each design are shown in Table 10 along with the predicted estimates produced by the DACE model. To compare the accuracy of the underlying model, the estimates were based on the model hyperparameters produced by the *MLE* optimization during the previous (i.e. 299th) step. The difference between the calculated and estimated values are shown in absolute as well as a percentage change from the actual value.

For the majority of objective functions, the model was seen to perform extremely well, with only the $SKEH$-based model showing any notable difference to the calculated
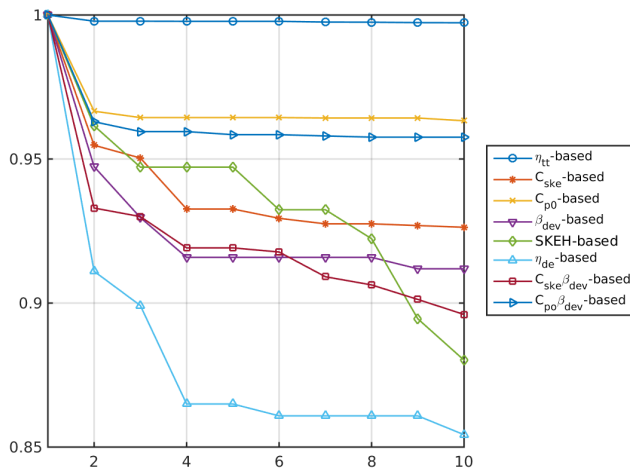
Figure 9. Normalized cumulative minimum objective function values for iterations 1 - 300 (every 30th point plotted)

results. The poor relative performance of the $SKEH$-based objective function was of significance because this metric was also noted to display the poorest overall performance in terms of the initial model fitting metrics (Table 6) whilst the difficulties with the metric were also evidenced in the overall poor convergence properties for the design as discussed previously.

Conclusions

This paper detailed the design and implementation of a fully autonomous non-axisymmetric turbine endwall design procedure, which, as a result of its use of the DACE surrogate modelling technique, was able to search for the global optima of various cost functions despite the use of reasonably high fidelity CFD as part of the process.

The final endwall shapes, when examined in conjunction with plots of the reduction in the normalized cost function magnitude, showed a clear bias towards the 'simple' objective functions in terms of convergence characteristics, with those formulated using either the aerodynamic loss ($C_{p0,rel}$) or similar metrics (such as the rotor efficiency, η_{tt}) exhibiting the most preferable convergence characteristics. Similarly, those objective functions which were based on one or more of the CFD solution primitive values (such as the flow angles or velocities) appeared to show less favourable convergence characteristics.

In addition, when the DACE model predictions were compared with the CFD predictions for the final optimization point, a clear connection between the overall predictive accuracy of the underlying surrogate model and the convergence characteristics for that objective function was noted.
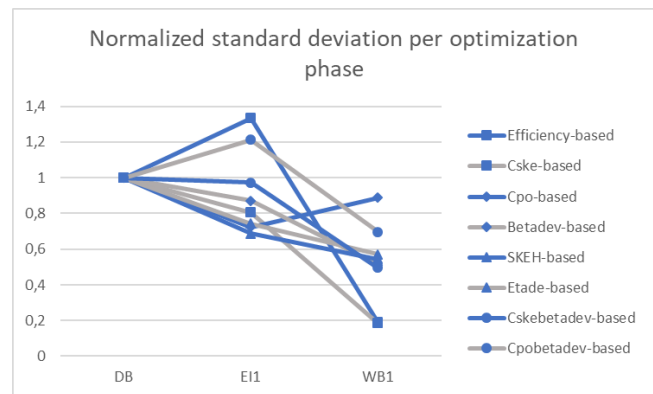
Supplemental material

The source code for the endwall design and optimization routine discussed in this paper may be downloaded at:- *https://github.com/icojb25/TurbineOpti.*
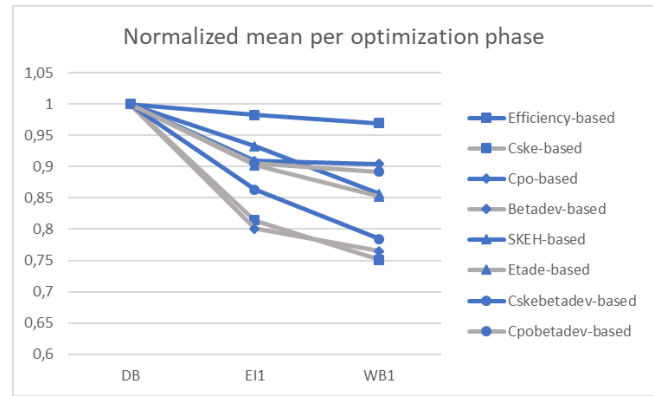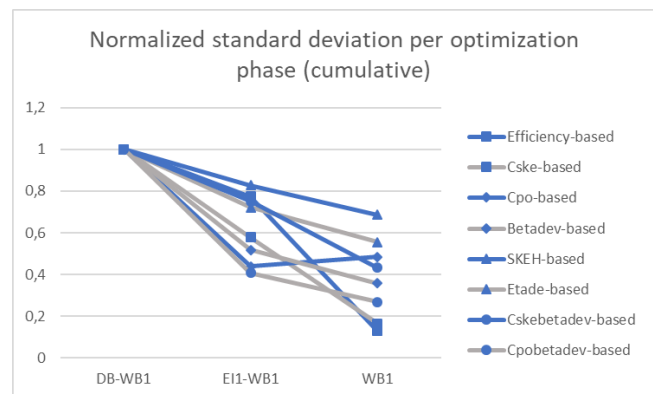
(a) Normalized mean (per phase)
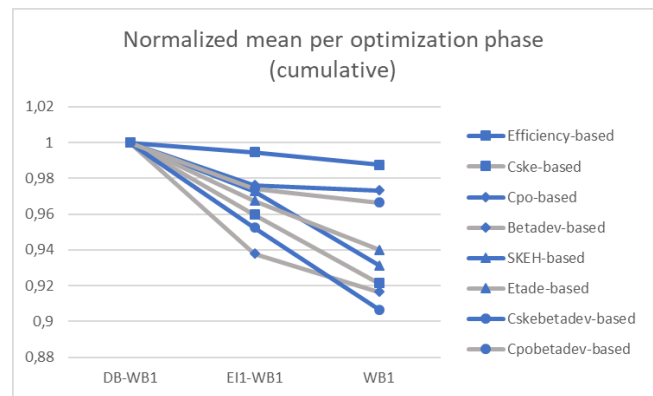
(b) Normalized mean (cumulative)

(c) Normalized std dev (σ) (per phase)

(d) Normalized std dev (σ) (cumulative)

Figure 10. Changes in normalized mean and standard deviation of all infill points for each endwall calculated per optimization phase and cumulatively

Declaration of conflicting interests

The author(s) declare no potential conflicts of interest with respect to the research, authorship, and / or publication of this article.

References

1. Ingram G. *Endwall profiling for the reduction of secondary flow in turbines*. PhD Thesis, School of Engineering, University of Durham, 2003.

2. Snedden G. *The application of non-axisymmetric endwall contouring in a 1 1/2 stage, rotating turbine*. PhD Thesis, School of Engineering, University of Durham, 2011.

3. Rose M. Non-axisymmetric endwall profiling in the hp ngv's of an axial flow gas turbine. In *Proceedings of the International Gas Turbine and Aerospace Congress and Exposition. The Hague, Netherlands. June 13-16*. 94-GT-249, ASME.

4. Harvey N, Rose M, Taylor M et al. Nonaxisymmetric turbine end wall design: Part i - three-dimensional linear design system. *Journal of Turbomachinery* 2000; 122: 278–285.

5. Hartland J, Gregory-Smith D, Harvey N et al. Nonaxisymmetric turbine end wall design: Part ii - experimental validation. *Journal of Turbomachinery* 2000; 122(2): 286–293.

6. Brennan G, Harvey N, Rose M et al. Improving the efficiency of the trent 500 hp turbine using non-axisymmetric end walls: Part 1 turbine design. In *Proceedings of ASME Turbo Expo 2001, New Orleans, USA*.

7. Rose M, Harvey N, Seaman P et al. Improving the efficiency of the trent 500 hp turbine using non-axisymmetric end walls. part ii: Experimental validation. In *Proceedings of ASME Turbo Expo 2001, New Orleans, USA*.

8. Harvey N, Brennan G, Newman D et al. Improving turbine efficiency using non-axisymmetric end walls: Validation in the multi-row environment and with low aspect ratio blading. In *Proceedings of ASME Turbo Expo 2002, Amsterdam, The Netherlands*. ASME, ASME, pp. 119 – 126.

9. Nagel M and Baier RD. Experimentally verified numerical optimization of a three-dimensional parameterized turbine vane with non-axisymmetric end walls. *Journal of Turbomachinery* 2005; 127: 380–387.

10. Praisner T, Allen-Bradley E, Grover E et al. Application of non-axisymmetric endwall contouring to conventional and high-lift turbine airfoils. In *AMSE Turbo Expo 2007: Power for Land, Sea and Air. May 14-17, 2007, Montreal, Canada*. GT2007-27579, ASME.

11. Germain T, Nagel M, Raab I et al. Improving efficiency of a high work turbine using nonaxisymmetric endwalls - part 1: Endwall design and performance. In *Proceedings of GT2008: ASME Turbo Expo 2008: Power for Land, Sea and Air*. GT2008-50469, ASME, ASME.

12. Schuepbach P, Rose M, Gier J et al. Non-axisymmetric end wall profiles including fillet radii in a 1.5 stage axial flow turbine. In *Proceedings of the 8th European Conference on Turbomachinery Fluid Dynamics and Thermodynamics (ETC '09)*. Graz, Austria.

13. MacPherson R and Ingram G. Endwall profile design for the durham cascade using genetic algorithms. In *Seventh South African Conference on Computational and Applied Mechanics*.

14. Poehler T, Gier J and Jeschke P. Numerical and experimental analysis of the effects of non-axisymmetric contoured stator endwalls in an axial turbine. In *ASME Turbo Expo 2010: Power for Land, Sea and Air. Glasgow, UK*.

15. Vazquez R and Fidalgo V. The effect of reynolds and mach number on end-wall profiling performance. In *Proceedings of ASME Turbo Expo 2010: Power for Land, Sea and Air, Glasgow, UK*. ASME, ASME.

16. McIntosh J, MacPherson R, Ingram G et al. Profiled endwall design using genetic algorithms with different objective functions. In *ASME Turbo Expo Vancouver, Canada, June 6-11*. ASME, ASME.

17. Hilfer M, Ingram G and Hogg S. Endwall profiling with tip clearance flows. In *Proceedings of ASME Turbo Expo 2012: GT2012, June 11-15, Copenhagen, Denmark*. GT2012-68488, ASME, ASME.

18. Bergh J, Snedden G and Meyer C. Optimization of non-axisymmetric end wall contours for the rotor of a low speed, 1 1/2 stage research turbine with unshrouded blades. In *Proceedings of ASME Turbo Expo 2012: GT2012, June 11-15, Copenhagen, Denmark*. GT2012-68569, ASME, ASME.

19. Miyoshi I and Higuchi S. Improving the performance of a high pressure gas turbine stage using a profiled endwall. In *Proceedings of ASME Turbo Expo 2013: Turbine Technical Conference and Exposition*. GT2013-95148, ASME, ASME.

20. Poehler T, Niewoehner J, Jeschke P et al. Investigation of non-axisymmetric endwall contouring and 3d arifoil design in a 1.5 stage axial turbine part 1: Design and novel numerical analysis method. In *Proceedings of ASME Turbo Expo 2014. Dusseldorf, Germany*. GT2014-26784, ASME, ASME.

21. Gregory-Smith D, Bagshaw D, Ingram G et al. Using profiled endwalls, blade lean and leading edge extensions to minimise secondary flow. In *ASME Turbo Expo 2008: Power for Land, Sea and Air. June 9-13, 2008. Berlin, Germany*. GT2008-50811, ASME, ASME.

22. Holland J. *Adaptation in natural and artificial systems: An introductory analysis with applications to biology, control and artificial intelligence*. 1st ed. University of Michigan Press, 1975.

23. Jones D, Schonlau M and Welch W. Efficient optimization of expensive black-box functions. *Journal of Global Optimization* 1998; 13: 455–492.

24. Sacks J, Welch W, Mitchell T et al. Design and analysis of computer experiments. *Statistical Science* 1989; 4(4): 409–435.

25. Krige D. A statistical approach to some basic mine valuation problems on the witwatersrand. *Journal of the Chemical, Metallurgical and Mining Society of South Africa* 1951; 52: 119–139.

26. Sasena M, Papalambros P and Gooverts P. Exploration of metamodelling sampling criteria for constrained global optimization. *Eng Opt* 2002; 34: 263–278.

27. Watson A and Barnes R. Infill sampling criteria to locate extremes. *Mathematical Geology* 1995; 27(5): 589–608.

28. Sasena M, Papalambros P and Gooverts P. Metamodeling sampling criteria in a global optimization framework. In *8th AIAA/USAF/NASA/ISSMO Symposium on Multidiscplinary Analysis and Optimization*. AIAA-2000-4921, Long Beach, CA: AIAA.

29. ANSYS Inc. *ANSYS ICEM CFD User's Manual, Canonsburg PA, 15317, USA*.

30. ANSYS Inc. *ANSYS Fluent Theory Guide, Southpointe 275 Technology Dr, Canonsburg PA, 15317, USA*.

31. Martin J and Simpson T. On the use of kriging models to approximate deterministic computer models. In *ASME 2004*

International Design Engineering Technical Conferences and Computers and Information in Engineering Conference. Salt Lake City, Utah. USA. September 28 - October 2, 2004. ASME.

32. Storn R and Price K. Differential evolution - a simple and effective adaptive scheme for global optimization over continuous spaces. Technical Report TR-95-012, ICSI, 1995.

33. Kok S. The asymptotic behaviour of the maximum likelihood function of kriging approximations using the gaussian correlation function. In *EngOpt 2012 - International Conference on Engineering Optimization. Rio de Janeiro, Brazil*.

34. Lophaven S, Nielsen H and Sondergaard J. Aspects of the matlab toolbox dace. Technical Report IMM-REP-2002-13, Technical University of Denmark, DK-2800 Kongens Lyngby, Denmark, 2002.

35. Menter F. Two-equation eddy-viscosity turbulence models for engineering applications. *American Institute of Aeronautics and Astronomics Journal* 1994; 32(8): 1598 – 1605.

36. Menter F, Smirnov P, Liu T et al. A one-equation local correlation-based transition model. *Flow, Turbulence and Combustion* 2015; : 1–37.

37. Snedden G, Dunn D and Ingram G. On and off-design performance of a model rotating turbine with non-axisymmetric endwall contouring and a comparison to cascade data. *The Aeronautical Journal* 2018; Volume 122, Issue 1259: 646–665.

38. NREC. *The design and performance analysis of axial-flow turbines: Volumne 1 and 2*. Northern Researach and Engineering Corporation, 1972.

Nomenclature

σ, σ^2 standard deviation, DACE model variance

$C_{\dot{m}}$ mass flow coefficient

Cr differential evolution cross-over rate

F differential evolution scaling factor

H flow helicity, $\vec{v} \cdot (\boldsymbol{\nabla} \times \vec{v})$

P blade pitch

P_h DACE model smoothness parameter

R_0 nominal turbine hub radius

S blade span

SKE secondary kinetic energy

$SKEH$ secondary kinetic energy helicity

U blade speed

V velocity magnitude (absolute)

$C_{p0,rel}$ total pressure loss coefficient (relative)

C_{ske} coefficient of secondary kinetic energy

Λ degree of reaction, $\phi/2(\tan \beta_3 - \tan \beta_2)$

β flow angle (relative)

β_{dev} flow deviation from design angle (relative)

δr change in turbine hub radius

$\dot{m}, \dot{m}_{ref}$ mass flow, reference mass flow

ϵ_m machine epsilon / accuracy

η_{de} design efficacy

η_{tt} total-total efficiency

κ matrix condition number

$\lambda_{min/max}$ minimum / maximum eigenvalues

$\mathcal{L}_c$ concentrated likelihood function

$\mathbf{R}$ DACE model correlation matrix

$\tilde{\mathbf{R}}$ DACE model correlation matrix (regularized)

ν DACE model regularization nugget

$\overline{Y}$ mass-averaged quantity

ϕ flow coefficient, $\frac{V_{ax}}{U}$

ψ loading coefficient, $2\phi(\tan \beta_2 + \tan \beta_3)$

ψ_1 phase angle of endwall curve 1

ρ fluid density

θ circumferential coordinate

φ endwall curve phase shift

$\vec{\theta}$ DACE model hyperparameters

$\vec{v}$ flow velocity (absolute)

$\vec{x}^i, \vec{x}^j$ DACE i^{th}, j^{th} input points

$\vec{x}^p$ DACE prediction point

a_n, b_n Fourier series coefficients

b_h DACE model range parameter

c endwall curve amplitude

d DACE model weighted distance between design points

k number of harmonics, problem dimensionality

n endwall curve period, no. of DACE model datapoints

p, p_0 static / stagnation pressure

w rotor specific work

y DACE model objective function prediction

Subscripts

$1/2/3$ *NGV* inlet / rotor inlet / rotor outlet

ax axial

d design quantity

is isentropic

k endwall curve number

rad radial

rel relative

sec secondary